

1                   **MECHANICAL CHARACTERISATION OF ADDITIVELY MANUFACTURED**  
2                   **ELASTOMERIC STRUCTURES FOR VARIABLE STRAIN RATE APPLICATIONS**

3  
4  
5           **Michael Robinson<sup>a</sup>, Shwe Soe<sup>a</sup>, Richard Johnston<sup>b</sup>, Rhosslyn Adams<sup>a</sup>, Benjamin**  
6           **Hanna<sup>a</sup>, Roy Burek<sup>a,c</sup>, Graham McShane<sup>d</sup>, Rafael Celeghini<sup>e</sup>, Marcilio Alves<sup>f</sup>, Peter**  
7   **Theobald<sup>a\*</sup>**

8  
9  
10   <sup>a</sup> High Value Manufacturing Research Group, Cardiff School of Engineering, Cardiff  
11   University, Wales, United Kingdom.

12   <sup>b</sup> Advanced Imaging of Materials (AIM) Facility, College of Engineering, Swansea University,  
13   UK;

14   <sup>c</sup> Charles Owen, Royal Works, Croesfoel Industrial Park, Wrexham, UK.

15   <sup>d</sup> Department of Engineering, Trumpington Street, Cambridge University, UK.

16   <sup>e</sup> Centre of Engineering, Modelling and Applied Social Science (CECS), Federal University of  
17   ABC (UFABC), Brazil.

18   <sup>f</sup> Department of Mechatronics and Mechanical Systems Engineering. Group of Solid  
19   Mechanics and Structural Impact, University of São Paulo (USP), Brazil

20

21

22   **\* Corresponding Author:** Dr P S Theobald, Cardiff School of Engineering, Cardiff  
23   University, The Parade, Cardiff, CF24 3AA, UK.

24

25 **Abstract**

26

27 Additive manufacturing (AM) enables production of geometrically-complex elastomeric  
28 structures. The elastic recovery and strain-rate dependence of these materials means they  
29 are ideal for use in dynamic, repetitive mechanical loading. Their process-dependence, and  
30 the frequent emergence of new AM elastomers, commonly necessitates full material  
31 characterisation; however, accessing specialised equipment means this is often a time-  
32 consuming and expensive process. This work presents an innovative equi-biaxial rig that  
33 enables full characterisation via just a conventional material testing machine (supplementing  
34 uni-axial tension and planar tension tests). Combined with stress relaxation data, this  
35 provides a novel route for hyperelastic material modelling with viscoelastic components.  
36 This approach was validated by recording the force-displacement and deformation histories  
37 from finite element modelling a honeycomb structure. These data compared favourably to  
38 experimental quasistatic and dynamic compression testing, validating this novel and  
39 convenient route for characterising complex elastomeric materials. Supported by data  
40 describing the potential for high build-quality production using an AM process with low  
41 barriers to entry, this study should serve to encourage greater exploitation of this emerging  
42 manufacturing process for fabricating elastomeric structures within industrial communities.

43

44 **Keywords**

45 *Elastomeric Polymer Characterisation; Hyperelastic; High strain-rate FEA analysis; Cellular*  
46 *Structures; Viscoelastic*

47

48 **1. Introduction**

49

50 Thermoplastic elastomers (TPEs) are co-polymeric materials that exhibit both thermoplastic  
51 and elastomeric properties, with their functional advantages meaning they are used across a  
52 broad range of applications. Tooling costs associated with traditional manufacturing  
53 methods typically constrains TPE production to high volume components only, limiting  
54 opportunities to lever a performance advantage. The emergence of additive manufacturing  
55 (AM), with unrivalled design freedom and the economic-viability of one-off production,  
56 provides new opportunities to employ TPEs in environments demanding low-volume, high-  
57 performance, or both.

58

59 Finite element analysis (FEA) simulations are well-established in the design, testing and  
60 evaluation of new and novel applications. Emerging techniques including topology  
61 optimisation and cellular lattice generation have supplemented this process, guiding  
62 designers with an over-riding objective function that prescribes the ultimate mechanical  
63 performance [1, 2]. These approaches are now being used in a series of, predominantly  
64 metal-based, weight-sensitive applications [3, 4].

65

66 The success of optimisation techniques is inherently governed by the accuracy of the  
67 material behaviour defined within the simulation. Where the analytical descriptor of a  
68 material's behaviour correlates poorly with its physical performance, the simulation will likely  
69 deliver an inaccurate solution. TPEs, which exhibit a hyper-elastic (HE) response, can be  
70 particularly challenging to characterise due to phenomena such as the Mullin's effect [5],  
71 where stress-softening occurs based on the previous level of strain experienced by the  
72 material. This results in the material's primary response (i.e. that to the first loading) differing  
73 from that of subsequent loading cycles (i.e. the stabilised response). Determining if one, or

74 both, of these responses are of importance to an application, is key to accurately simulating  
75 HE events.

76

77 The non-linear HE response of TPE materials means they cannot be characterised by a  
78 single data-point. Established constitutive models comprise a series of coefficients  
79 associated with strain energy density functions capturing the variation of stress versus strain,  
80 with advanced FEA software enabling the end-user to identify the model with the strongest  
81 correlation to experimental data. Coefficients describing AM-produced materials typically  
82 differ from traditionally manufactured equivalents [6, 7]. Whilst characterisation of AM  
83 metallic structures have now been reported [8, 9], no studies quantify the rate-dependant  
84 behaviour of HE AM material properties when simulating dynamic events. The technical  
85 demands of such characterisation, with laboratories rarely having the requisite facilities  
86 including a stand-alone equi-biaxial testing apparatus [10], risks constraining the  
87 development and uptake of new TPE AM filaments and powders.

88

89 This study describes a novel experimental approach to characterise TPE materials for  
90 applications experiencing strain-rates in excess of quasistatic conditions (referred to as  
91 dynamic strain-rate applications), using solely a commonplace uniaxial testing machine.  
92 Primary, stabilised and rate-dependant responses were captured and then fitted with an  
93 appropriate HE/viscoelastic material model. Computational analysis of an exemplar TPE AM  
94 structure within a dynamic strain-rate environment demonstrates both the validity of this  
95 characterisation process, and the potential to enable high-performance designs.

96 **2. Materials and Methods**

97

98 Uniaxial, equi-biaxial, and planar tension data was collected to define the HE behaviour; for  
99 both primary and stabilised responses. Rate-dependant behaviour was defined by stress  
100 relaxation data. For uniaxial, equi-biaxial and planar tests, strain in the gauge area was  
101 measured using non-contact video-extensometry (iMetrum CAM028, UK). All stresses and  
102 strains are reported as nominal (i.e. engineering) data.

103

104 2.1. Materials

105

106 *Table 1. Printing parameters used for this study*

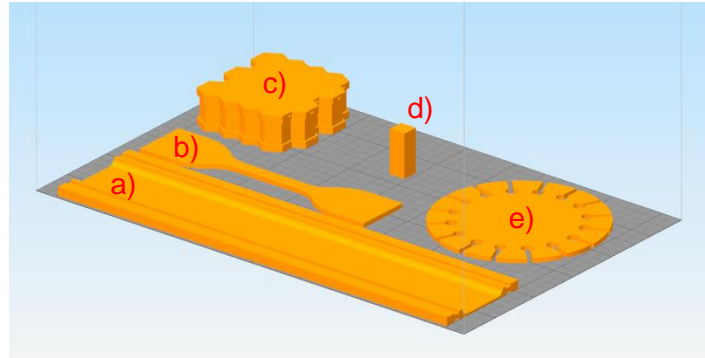
Nozzle Diameter	0.4 mm	Extrusion Multiplier	1.4
Print speed	2000mm/min	Layer Height	100
Bed Temperature	40C	Active cooling	Yes
Extruder Temperature	210	Infill extrusion width	125%

107

108 SOLIDWORKS (Dassault Systems, France) was used to design coupons for each test  
109 method that were manufactured in NinjaFlex (NinjaTek, US), a readily available TPE filament  
110 selected as an exemplar AM material. A fused filament fabrication printer was used (2017  
111 Flashforge Creator Pro printer), retrofitted with high-specification extrusion control (Diabase  
112 Engineering, USA) and using processing parameters tuned to achieve a high extrusion  
113 density. **Simplify3D (Simplify3D, US) was used to alter print settings and slice the .STL files  
114 for printing.** The common rectilinear pattern was adopted for in-filling the parts and X-ray  
115 microscopy (XRM)/microcomputed tomography ( $\mu$ CT) was used to confirm successful fusing  
116 of the infill extrudate. Infill was set to 100% and the extrusion settings tuned to ensure fusing  
117 of the extrudate, allowing confidence that the infill pattern would have minimal effect on

118 experimental results. A honeycomb was also designed and manufactured for use as a case  
119 study to demonstrate the validity of this novel characterisation methodology, with part quality  
120 assessed via  $\mu$ CT. Print orientation is shown in Figure 1.

121



122 *Figure 1. Test part build orientations. a) Planar, b) Uniaxial, c) Honeycomb geometry, d)*  
123 *Cuboid for  $\mu$ CT Scanning, e) Equi-biaxial*

124

## 125 2.2. Methods

126

127 A preliminary simulation was undertaken to establish the minimum/maximum strains  
128 experienced during the loading of the honeycomb structure. This allowed identification of the  
129 appropriate cycled strain during mechanical testing, used to describe the stabilised response  
130 of the TPE material. A linear elastic model [11] was applied to the honeycomb structure,  
131 which was compressed within ABAQUS to densification. The recorded strain was  
132 approximately +/- 0.3 throughout the simulated densification of the honeycomb (to ~60% of  
133 its original height). This guided the adoption of an upper strain threshold of 0.4 for  
134 mechanical testing.

135 *During the preliminary simulation, a mesh sensitivity study was undertaken. Varying the*  
136 *element size from one-quarter, to twice, the wall thickness, achieved near-identical force-*  
137 *displacement curves, and predicted energies also showed little deviance when altering mesh*

138 size. This lack of deviance is consistent with other literature on dynamic compression of  
139 cellular structures [12].

140 Five samples were manufactured for each test setup described in section 2.2.1.

141

## 142 *2.2.1. Mechanical Testing*

143

### 144 *Uniaxial (Tension) Testing*

145

146 Testing was performed using an electromechanical uniaxial testing machine (Zwick Z50,  
147 Germany), following ISO 37 [13] with a reduced crosshead speed (100mm/min), to minimise  
148 strain rate sensitivity. Test coupons were designed and fabricated as per tensile testing  
149 specimen type 1 [13]. Investigation was performed over cyclical loading to 0.4 strain.

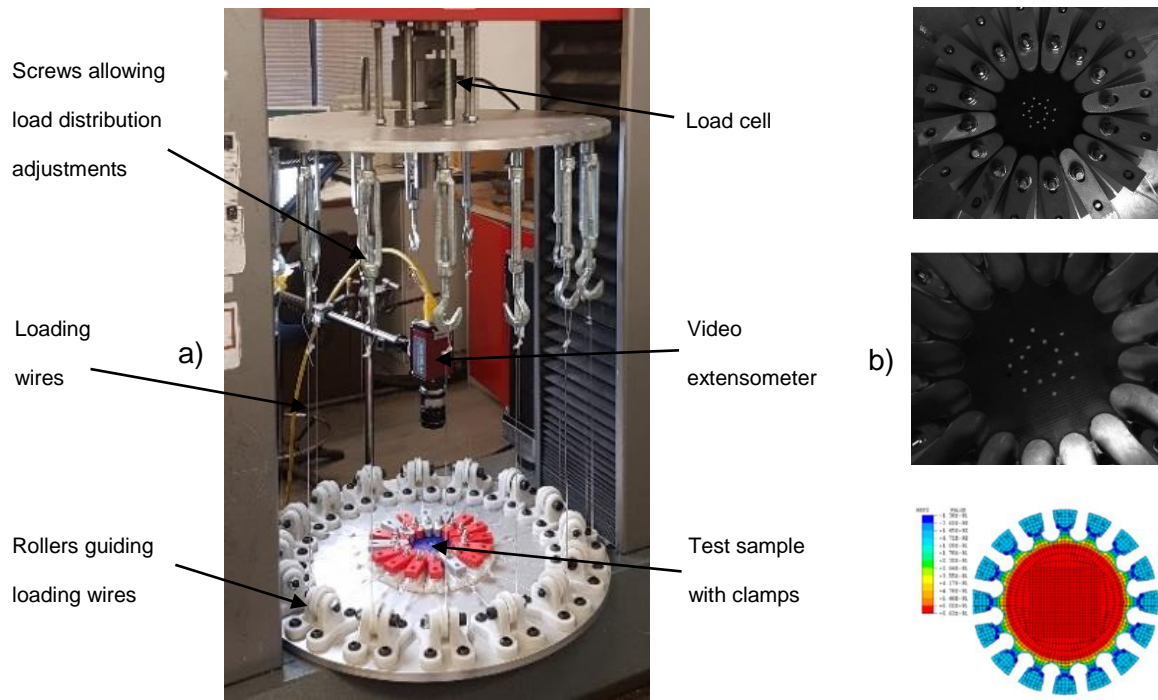
150

### 151 *Equi-Biaxial (Tension) Testing*

152

153 An equi-biaxial test apparatus was designed and built in-house, to enable multi-axial data  
154 generation from a single uniaxial testing machine. Novel test coupons were designed and  
155 manufactured, including 16 clamping tabs that enabled uniform application of a multi-axial  
156 load, generating equi-biaxial strain in the coupon centre (Figure 2 a & b). These test  
157 specimens have been shown to be appropriate for equi-biaxial testing [10], with FE analysis  
158 showing little influence of geometry on the state of stress in the central gauge section.  
159 Machine parameters and cycled strain were consistent with the uniaxial setup.

160



161 *Figure 2: a) Equi-biaxial test rig, b) Stretching of Equi-biaxial sample in this study, and FEA*  
 162 *validation of sample performed by Day, J. (reproduced from [10])*

163

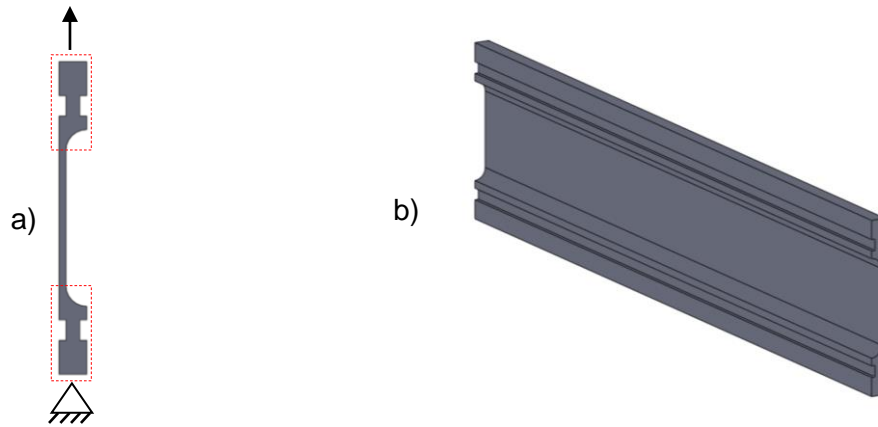
164 *Planar (Tension) Testing*

165 Shear data is valuable when modelling hyperelastic materials, which is derived from planar  
 166 tension testing [14, 15]. Novel planar coupons were designed to include ridges, which  
 167 improved gripping and ensured load distribution into the test gauge area (Figure 3 a & b).  
 168 Machine parameters and cycled strain were again consistent with the uniaxial setup.

169

170





171 *Figure 3: a) Side profile highlighting ridges/added geometry on planar sample, b) 3D*  
 172 *visualisation of planar sample*

173

174 *Stress Relaxation Testing*

175

176 The uniaxial test geometry was used to measure stress relaxation, performed at the  
 177 maximum available cross-head speed (600mm/min), to a strain of 0.4 and followed by a  
 178 100s relaxation period. Stress relaxation experiments cannot achieve an instantaneous step  
 179 input and will always include an initial loading ramp, as well as inertial effects from the test  
 180 equipment loading. The user must compensate for these effects when analysing the data,  
 181 by back-calculating to a theoretical instantaneous load point, as has been performed here.

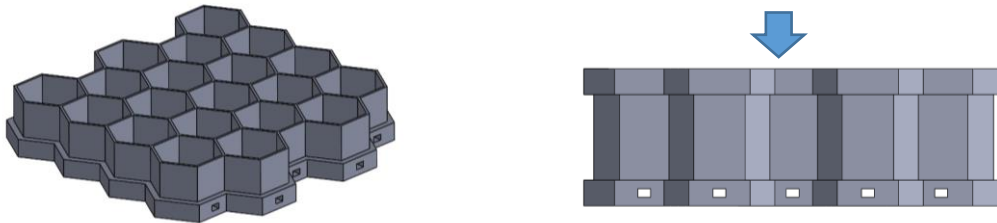
182 *Mechanical Testing of Exemplar TPE AM Honeycomb*

183

184 A NinjaFlex hexagonal honeycomb was designed and manufactured to validate the above  
 185 characterisation process and to demonstrate the potential of AM TPEs to produce structures  
 186 for high performance applications. The honeycomb structure consisted of a 4x5 unit cell,  
 187 with each cell having a side length of 5.8mm, 10mm height and 0.4mm wall thickness. Two  
 188 3mm thick solid sections were designed onto the upper and lower surfaces of the  
 189 honeycomb, to achieve well-defined boundary conditions. Exhaust channels (1mm

190 diameter) were designed in to the lower solid section, enabling release of air trapped within  
191 the honeycomb cavities during compression and impact testing.

192



193 *Figure 4. a) sectioned view of the honeycomb part, b) indication of load direction on part*

194

195 The honeycomb structure was cyclically compressed to densification (~60% of its original  
196 height) at 100mm/min (i.e. quasistatically). Industrial-strength adhesive tape (Tesa 64621)  
197 was used to adhere the solid sections to the compression platens, ensuring consistent  
198 boundary conditions. Dynamic testing was then performed to evaluate the relative  
199 performance of the TPE AM honeycomb in a dynamic strain rate environment. A guided  
200 drop tower (Instron 9250HV, US) was used to strike the honeycomb test geometry with a  
201 3.53kg impactor at 1.4 m/s. This velocity ensured the honeycomb compressed to >60% of  
202 its overall height. An in-line accelerometer (Kistler 8715A, Switzerland) was used to record  
203 the acceleration-time pulse. Boundary conditions were defined by: the lower solid section of  
204 the honeycomb geometry being adhered to the anvil and, the impactor and upper solid  
205 section of the honeycomb being covered with sandpaper. The impactor was released from  
206 0.01m, allowing dynamic compression of the honeycomb to 60% of its original height.  
207 Acceleration-time pulses were converted using standard formulae into force-displacement  
208 and displacement-time data.

209

210 *Statistical Analysis*

211

212 Results of each test method are displayed as a mean value, with error bars representing the  
213 standard deviation (SD). All testing was performed through 5 cycles/impacts, to account for  
214 stress softening behaviour in the material, which decreased markedly after the second cycle  
215 and was cycled a further three times to ensure a stabilised response.

216

217 *2.2.2. Computational Analysis and Validation*

218

219 ABAQUS 6.14 (Dassault Systems, France) was used first to curve-fit an appropriate material  
220 model to the primary and secondary responses (for dynamic simulations the viscoelastic  
221 component was added to these material models), before enabling analysis of the primary  
222 and stabilised performance of an exemplar honeycomb structure. An appropriate material  
223 model was then selected based on the closest correlation with the test data. Explicit  
224 Dynamic analysis was used and, in addition to any other boundary conditions/interactions  
225 defined in the simulation, a global frictionless contact was defined to prevent self-penetration  
226 of the honeycomb. Incompressibility was assumed (i.e. Poisson's ratio = 0.475, as this is  
227 the maximum allowable in ABAQUS) and enhanced hourglass control implemented. Hyper-  
228 elastic material models were fitted separately to primary and stabilised datasets. Ogden 1<sup>st</sup>  
229 to 6<sup>th</sup> order, Polynomial 1<sup>st</sup> and 2<sup>nd</sup> order and Reduced Polynomial 1<sup>st</sup> to 6<sup>th</sup> order models  
230 were investigated for each state. The viscoelastic component of the material model was  
231 defined using normalised stress relaxation data, fitted by ABAQUS to a Prony series with  
232 0.001 minimum allowable root-mean-square error. A continuum element hex-dominated  
233 mesh was proliferated throughout with a seed equal to the measured **average** wall thickness  
234 of the honeycomb (0.45 mm); however, the 3mm thick upper and lower sections of the test

235 part were partitioned and given a larger (default) edge seed of 0.72 mm, to reduce the  
236 computational cost.

237

238 Due to the honeycomb walls being the same thickness as the extrusion nozzle, it was  
239 expected the manufactured wall thickness would increase. **Average** wall thickness was  
240 measured by  $\mu$ CT and used to update the honeycomb CAD for ABAQUS simulations. This  
241 ensured identical geometry of the simulated and mechanically tested parts.

242

243 Quasistatic compression was computationally modelled with the honeycomb component  
244 sandwiched between two rigid flat plates. The upper plate was tied to the upper solid  
245 section of the honeycomb and prescribed a deflection of 0.6mm, over 1s. The lower plate  
246 was fixed in space and tied to the lower honeycomb face. Viscoelastic material properties  
247 were not included, whilst a mass scaling of 20 considerably reduced simulation time with  
248 minimal influence on accuracy. The force-time and displacement-time histories were  
249 extracted from a reference node at the centre of the upper rigid plate, enabling direct  
250 comparison with mechanical testing results.

251

252 For simulated validation of the impact tests, the honeycomb was again sandwiched between  
253 two rigid flat plates in ABAQUS. The upper plate was now assigned a 3.53kg point mass  
254 and prescribed a pre-impact velocity observed during experimentation. A sliding frictional  
255 coefficient of 1 was defined between the upper honeycomb surface and adjacent plate, to  
256 represent a sandpaper-sandpaper contact. The lower honeycomb face was tied to the  
257 bottom plate, which was fixed in space. The acceleration-time and displacement-time  
258 histories were extracted from a reference node at the centre of the upper rigid plate, for  
259 comparison with mechanical testing results. Acceleration-time was converted to force-time  
260 using Newton's second law of motion.

### 2.2.3. X-ray Microscopy (XRM)/Microcomputed Tomography Scanning ( $\mu$ CT)

261  
262  
263  
264  
265  
266  
267  
268  
269  
270  
271  
272  
273  
274  
275  
276  
277  
278  
279  
280  
281  
282  
283  
284  
285  
286  
287

Porosity analysis was performed using a nominal cuboid structure (7.5 x 7.5 x 20 mm) manufactured from NinjaFlex and adopting the established processing parameters was analysed via XRM using a lab-based Zeiss Xradia 520 (Carl Zeiss XRM, Pleasanton, CA, USA) X-ray Microscope, using a CCD detector system with scintillator-coupled visible light optics, and tungsten transmission target. To achieve a higher resolution over the entire part height, the specimen was imaged along its 20 mm length at high resolution, using an overlap-scan and stitching procedure including five individual scans, with 15% overlap between each scan. An X-ray tube voltage of 60 kV and a tube current of 80  $\mu$ A were used, with an exposure of 1000 ms and a total of 3201 projections. An objective lens giving an optical magnification of 0.4 was selected with binning set to 2, producing an isotropic voxel (3-D pixel) sizes in the range 11.862  $\mu$ m. The tomograms were reconstructed from 2-D projections using a Zeiss commercial software package (XMReconstructor, Carl Zeiss), a cone-beam reconstruction algorithm based on filtered back-projection. XMReconstructor was also used to produce 2-D grey scale slices for subsequent analysis. **The boundary between pore (gas) and material of the smallest pores (< 2 voxel diameter) will be difficult to define, and therefore the segmentation process could introduce inaccuracies for those smaller pores. Therefore, a threshold size of 2 voxels was implemented and data below this size was excluded.**

The honeycomb sample was imaged using a lab-based Nikon XT H225 microfocus X-ray microtomography ( $\mu$ CT) system, with a 1.3 Megapixel Varian PaxScan 2520 amorphous silicon flat panel digital X-ray imager, in reflection mode with a molybdenum target. An X-ray tube voltage of 60 kV and a tube current of 130  $\mu$ A were used, with an exposure of 1000 ms and a total of 3015 projections, with a voxel (3-D pixel) size of 15.05  $\mu$ m. The tomograms were reconstructed from 2-D projections using a Nikon commercial software package

288 (CTPro version 3.0, Nikon Metrology), a cone-beam reconstruction algorithm based on  
289 filtered back-projection. The commercial software VGStudio Max 2.1.5 was used to view the  
290 reconstructed data and produce 2-D grey scale slices in TIFF format. These were imported  
291 into Avizo Software (ThermoFisher Scientific, Waltham, MA, USA), where post-processing  
292 including reorientation, binarization, and segmentation allowed extraction of pore size and  
293 volume. Honeycomb average wall thickness was measured using Vernier callipers, as well  
294 as digitally via the  $\mu$ CT data using SOLIDWORKS (Dassault Systems, France) and used to  
295 update the equivalent CAD/FEA model used for computational simulation.

296

297 **3. Results**

298

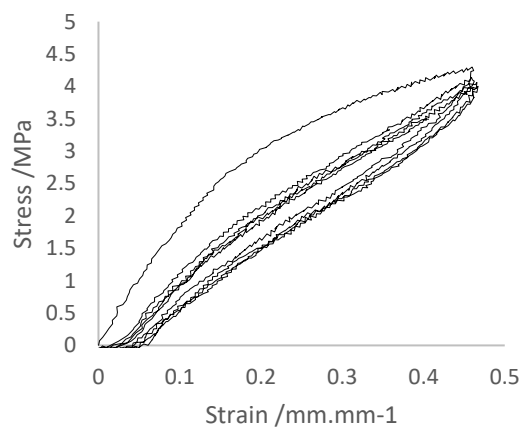
299 **3.1. Mechanical Testing**

300

301 The test results showed that the equi-biaxial response generated a higher stress than the  
302 planar response, which was greater than the uniaxial response, at any given strain (Figure  
303 6). This trend was consistent when considering both the primary and stabilised response.

304 Stress and strain for uniaxial and planar testing are presented based on the direction of the  
305 loading.

306



307 *Figure 5. cyclic behaviour of NinjaFlex under uniaxial loading*

308

309 **3.1.1. Primary HE response**

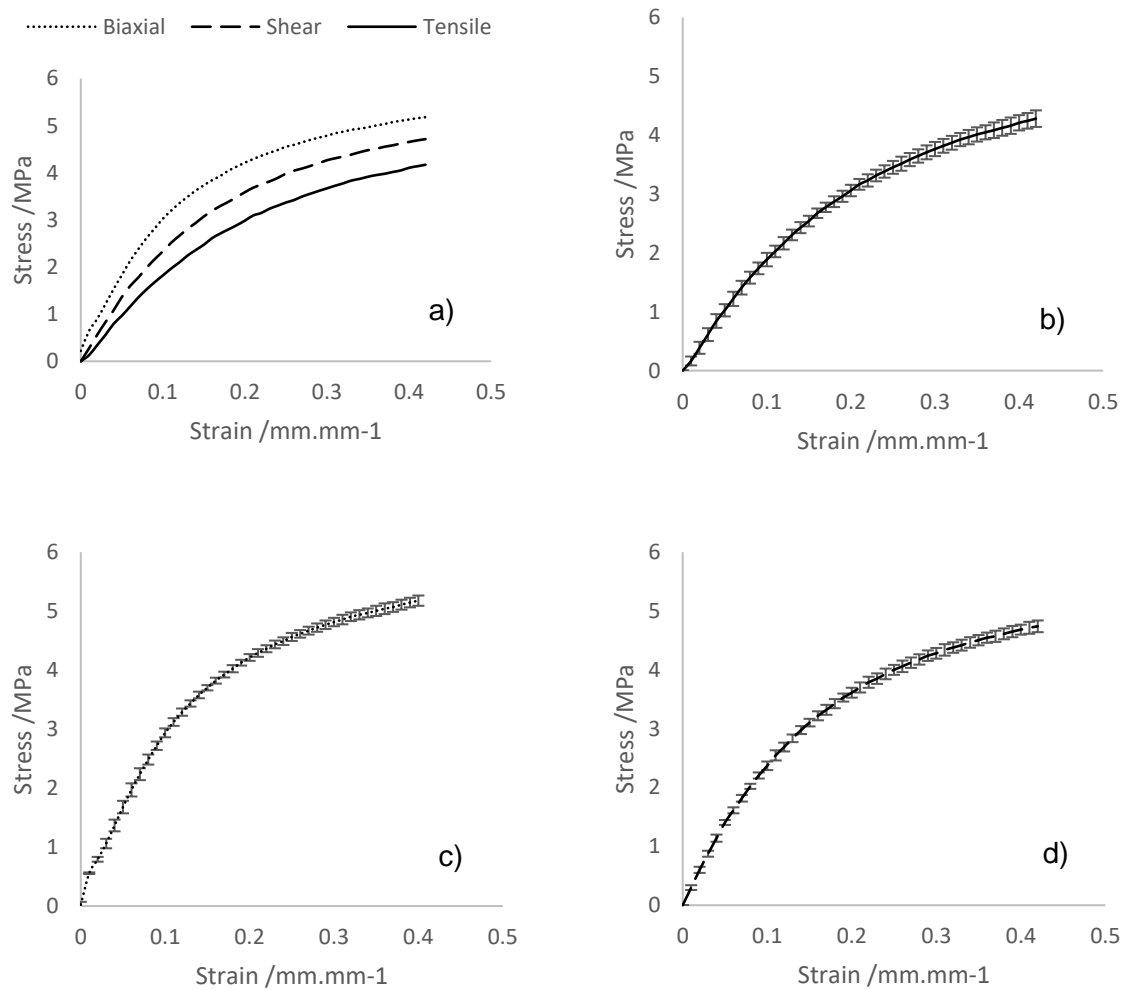
310

311 All datasets collected demonstrated non-linear behaviour typical of elastomeric materials.

312 Uniaxial testing gave an average initial modulus of 18.2MPa, when considering strains from  
313 0 to 0.1. The average initial planar modulus was 28% greater than uniaxial and the average  
314 initial equi-biaxial modulus 66% greater. At a strain of 0.4, uniaxial stress was 4.11 MPa,

315 planar stress was 4.66 MPa and equi-biaxial stress was 5.13MPa. The full data curves  
 316 showing the average mechanical test data are displayed in Figure 6.

317



318 *Figure 6 Mechanical testing for average primary response of: a) Combined data sets, b)*  
 319 *Uniaxial only, c) Equi-biaxial only, d) Planar only. Error bars = SD*

320

321 *3.1.2. Stabilised HE response*

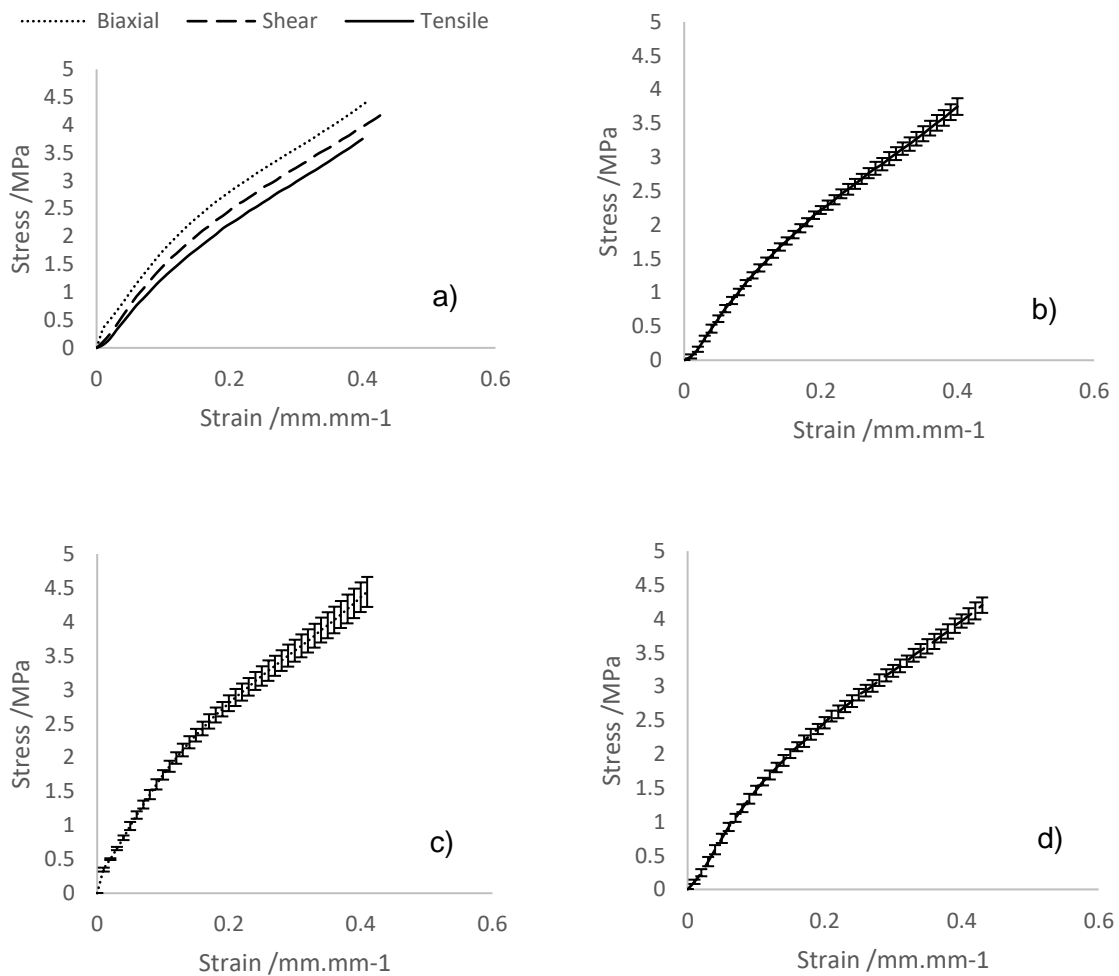
322

323 The planar data trend was closer to the uniaxial, than equi-biaxial, response. Uniaxial  
 324 testing gave an average initial modulus of 12.5MPa, when considering strains from 0 to 0.1.



325 The average initial planar modulus was 18% higher than uniaxial, and the average initial  
326 equi-biaxial modulus was 39% higher. At a strain of 0.4, uniaxial stress was 3.75 MPa,  
327 planar stress was 3.97 MPa and equi-biaxial stress was 4.36 MPa. Variance between the 5  
328 test samples for each stress state of the stabilised response was minimal, though larger than  
329 the primary response data (Figure 7).

330



331 Figure 7 Mechanical testing for the average stabilised response of: a) Combined data sets,  
332 b) Uniaxial only, c) Equi-biaxial only, d) Planar only. Error bars = SD

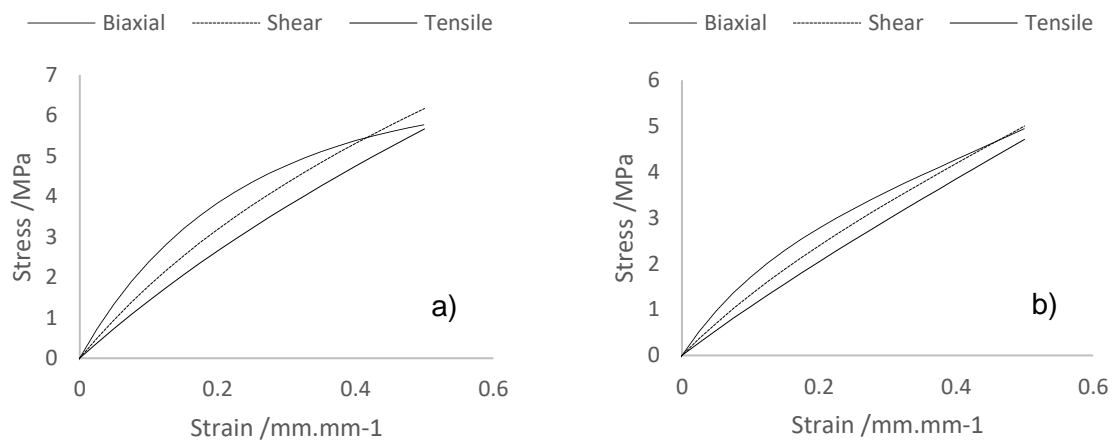
333

334 3.2. Curve-fitting

335

336 The ABAQUS-based curve fitting procedure for the primary and stabilised responses are  
337 presented in Figure 8. The Mooney-Rivlin model provided the most appropriate fit to the  
338 primary response, whilst the 2<sup>nd</sup> order Ogden model provided the best fit for the stabilised  
339 response.

340



341 *Figure 8 Graphs showing combined fit for: a) Primary response, b) Stabilised response*

342

343 The coefficients for the primary and stabilised responses material models are presented in  
344 Table 2 and Table 3. These models are mathematically stable, both fitting well to  
345 experimental extension data and sensibly predicting the compressive behaviour, for the  
346 positive and negative strain (+/- 0.3) estimated in the preliminary unit cell investigation  
347 (Section 2.2.1). It should be noted that outside of the predicted strain range both models  
348 become increasingly inaccurate.

349

350 Table 2 Primary response – Mooney-Rivlin material model coefficients

$C_{10}$ /MPa	$C_{01}$ /MPa
2.93	0.363

351

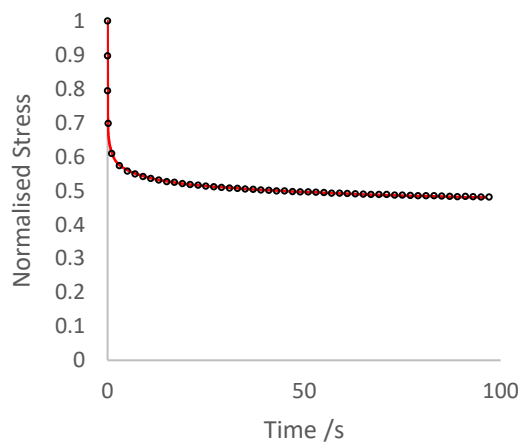
352 Table 3 Stabilised response – 2<sup>nd</sup> order Ogden material model coefficients

	$\mu_1$ /MPa	$\alpha_1$
1	12.2	1.87
2	8.41	1.19

353

354 Due to the specified low root mean square (RMS) error (0.001), the Prony series were  
355 calibrated closely to the experimental data (Figure 9). Examining the experimental data  
356 trend enables estimation of a long-term normalised modulus between 0.4 - 0.5. The Prony  
357 coefficients that define the curve presented in Figure 9 are quantified in Table 4.

358



359 Figure 9 Normalised uniaxial stress relaxation data, with Prony series curve fit

360

361 *Table 4 Viscoelasticity Prony series*

	<i>G /MPa</i>	<i>K /MPa</i>	<i>tau /s</i>
1	0.196	0.0000	1.27E-03
2	0.129	0.0000	8.30E-02
3	7.67E-02	0.0000	0.894
4	6.03E-02	0.0000	6.51
5	7.10E-02	0.0000	54.6

362

363

364

365

366

367

368

369

370

371

372

373

374

375

376

377

378

379

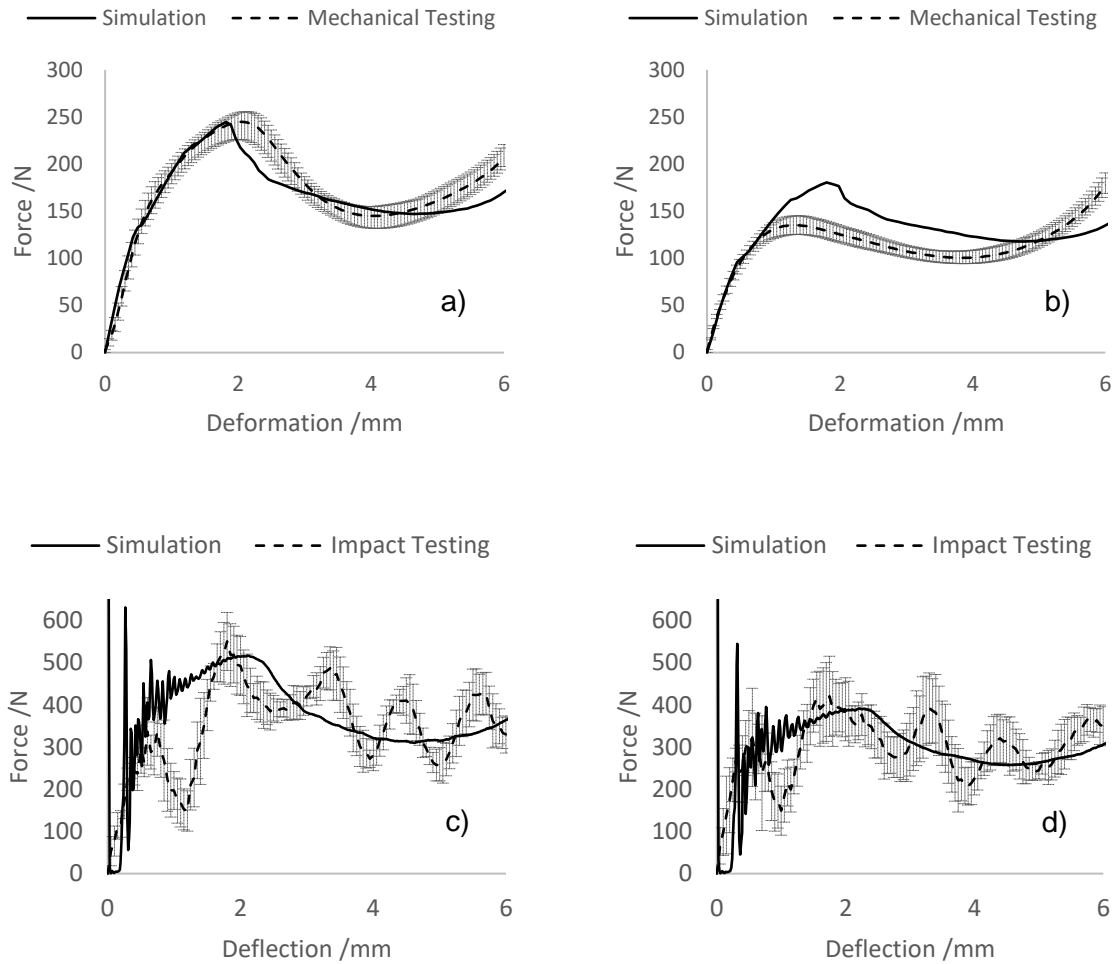
380

381

382

383

384 3.3. Honeycomb testing



385 *Figure 10 Honeycomb validation, plotting mechanical test data alongside related simulations:*

386 *a) Primary quasistatic, b) Stabilised quasistatic, c) Primary impact, d) Stabilised impact.*

387 *Error bars = SD*

388

389 *Quasistatic Honeycomb Compression*

390

391 The plateau region varies between experimental and simulation results, influencing the

392 energy absorbed by each structure prior to densification (Table 5). For the simulated

393 primary response, agreement exists between the experimental and simulation peak forces

394 and absorbed energy; however, an increase in peak displacement of 11% was observed in

395 the experimental results. The stabilised energies for the simulated and experimental results  
 396 were within 10% of one another.

397

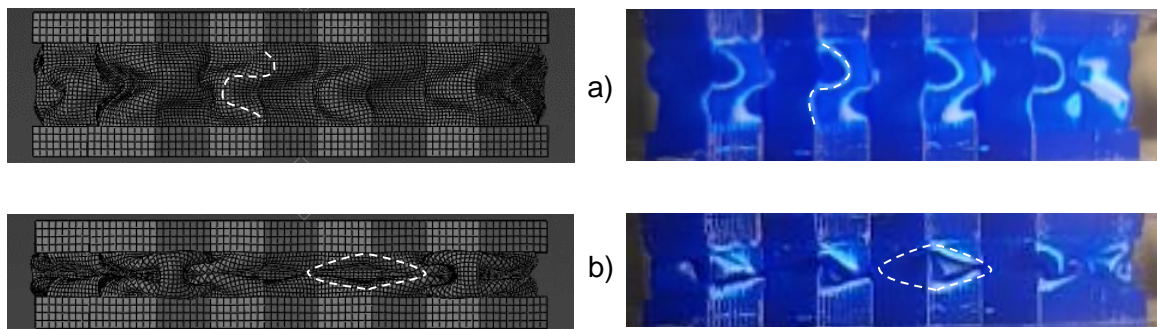
398 *Table 5 Peak quasistatic forces/displacements at commencement of plateau region + energy*  
 399 *absorbed by structure prior to densification*

	<i>Peak force pre- plateau /N</i>	<i>Displacement of peak force /mm</i>	<i>Energy absorbed by 6mm /J</i>
<i>Simulation Primary response</i>	245	1.82	1.00
<i>Mean Experimental Primary response</i>	245	2.05	1.04
<i>Simulation Stabilised response</i>	180	1.80	0.77
<i>Mean Experimental Stabilised response</i>	137	1.25	0.69

400

401 At 2mm, similar s-shaped and arrow-shaped deformation patterns were observed in  
 402 experimental testing and simulation (Figure 11). At greater levels of compression (2 –  
 403 6mm), the structure begins to fold inside itself with elongated diamond-shaped patterns.

404



405 *Figure 11 Comparison of simulated and experimental deformation during quasistatic*  
 406 *compression: a) 2mm, b) 6mm. Note, simulated images have been mirrored horizontally to*  
 407 *highlight deformation patterns.*

409

410 *Data describing the plateau regions is presented in*

411 Table 6. Experimental and simulated peak forces, displacements and energies absorbed  
 412 were all within 10% of one another for the dynamic primary and stabilised responses, except  
 413 the stabilised peak displacement, where the mechanical testing was 30% lower.

414

415 *Table 6 peak forces/displacements at commencement of plateau region + energy absorbed*  
 416 *by structure prior to densification dynamic*

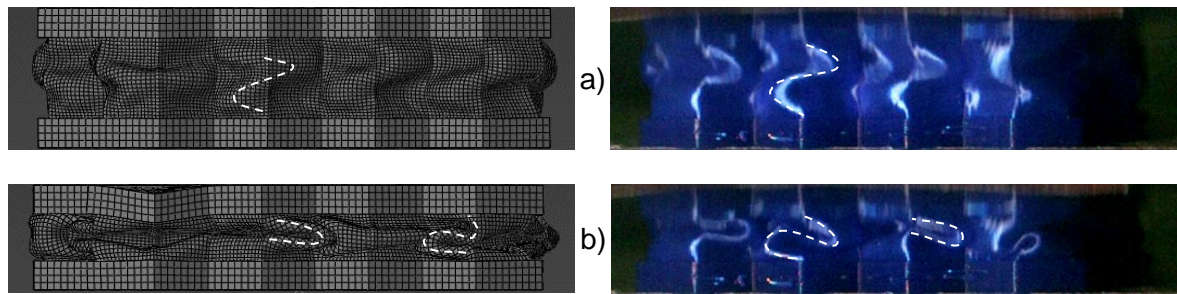
	<i>Peak force pre- plateau /N</i>	<i>Displacement of peak force /mm</i>	<i>Energy absorbed by 6.5mm /J</i>
<i>Simulation Primary response</i>	515	1.97	2.21
<i>Mean Experimental Primary response</i>	550	1.80	2.10
<i>Simulation Stabilised response</i>	391	2.20	1.75
<i>Mean Experimental Stabilised response</i>	420	1.75	1.77

417

418 Distinct s-shaped deformation was identified both in experimental testing and simulation, at  
 419 2mm compression (Figure 12). At 6mm, the experimental testing and simulation  
 420 demonstrated distinctive arrow-shaped and s-shaped deformation patterns; however, the  
 421 simulation also had outer walls folding into the centre of the structure, similar to observations  
 422 during quasistatic compression (Figure 11).

423

424



425 *Figure 12 Comparison of simulated and experimental deformation during impact: a) 2mm, b)*  
 426 *6mm. Note, simulated images have been mirrored horizontally to highlight deformation*  
 427 *patterns.*

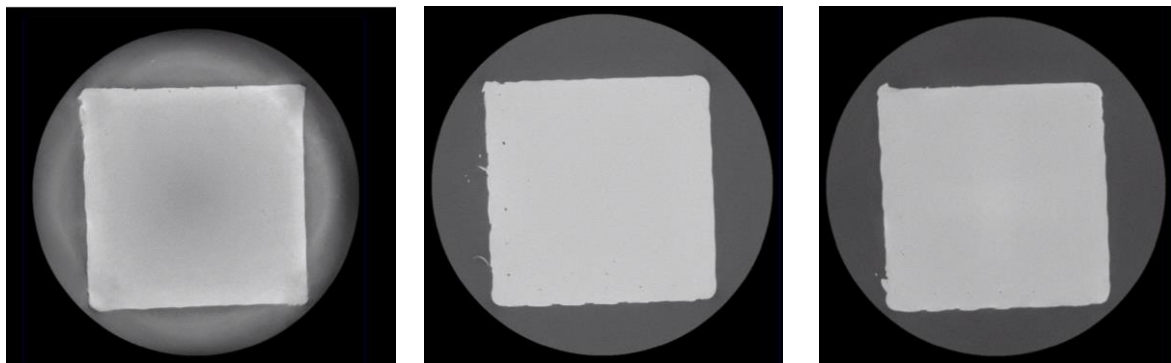
428

### 429 3.4. XRM/μCT Analysis

430

431 μCT scanning demonstrated that manufactured parts were largely homogenous, meaning  
 432 successful fusion of the extruded material (Figure 13). Additionally, the outline bounding the  
 433 internal rectilinear patterning was continuous, with no pores observed throughout its height.

434



435 *Figure 13 CT scanned cross-sections of cuboid geometry. Left-right: bottom, centre, top*

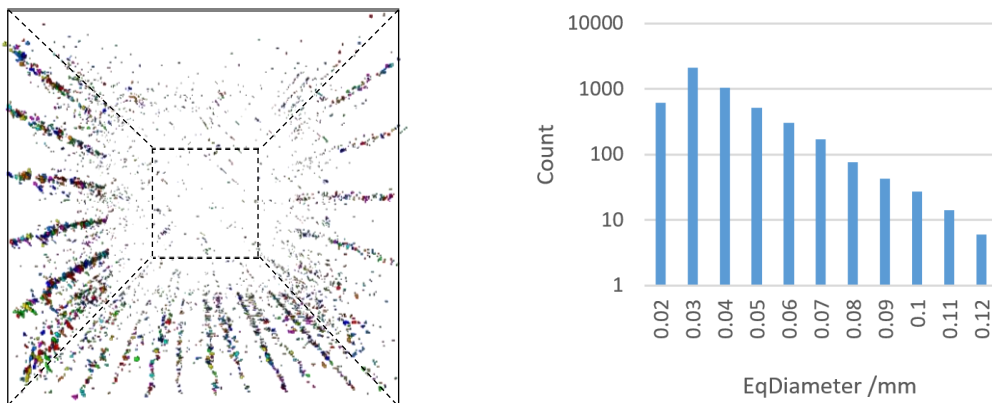
436

437 When analysing the pores within the scanned cuboid, those of equivalent diameter  $\leq 2$  voxels  
 438 (equivalent to 23.7 μm) were excluded. This was due to the potential lack of accuracy when  
 439 detecting pore edges of such small pores. Analysis of the remaining pores suggested the



440 cuboid was 99.97% dense, with an average pore size of 38  $\mu\text{m}$  and a max pore size of 119  
 441  $\mu\text{m}$ . Only ~10% of the pores were 60-119  $\mu\text{m}$ , and these appeared concentrated between  
 442 the rectilinear fill forming the cuboid centre and the outline forming the perimeter. The  
 443 distribution of the pores within the cuboid and the pore diameter histogram, are presented in  
 444 Figure 14. **A one-point perspective view down the length of the cuboid illustrates the pore**  
 445 **distribution (Figure 14a). The largest pores are located at the boundary of the outline and**  
 446 **the infill pattern, in lines running the height of the cuboid.**

447



448 *Figure 14 a) 3D image of pores within the cuboid structure, with a bounding outline to show*  
 449 *the approximate position of the cuboid exterior, b) histogram showing the effective length of*  
 450 *each pore*

451

452 The  $\mu\text{CT}$  scan and supporting vernier measurements of the honeycomb walls gave an  
 453 average thickness of 0.45mm (versus 0.4mm for the CAD design) **with a SD of 0.01 mm.**  
 454 **Based on the minimal deviation, the averaged value was used to simulate a part of constant**  
 455 **wall thickness within ABAQUS.** Some material could be observed drooping as the upper  
 456 surface 'bridged' over the honeycomb cell wall; however, this appeared minimal and did not  
 457 affect adhesion between these two features.

458

459 **4. Discussion**

460

461 The mechanical performance of TPE AM materials are known to vary with processing  
462 parameters, whilst new products regularly enter the market; hence, there is an increasing  
463 need to perform full characterisation, though the requisite equi-biaxial facilities remain  
464 scarce.

465

466 This study has demonstrated success with a novel approach to material characterisation,  
467 validated by the comparable trends achieved when experimentally and computationally  
468 compressing a honeycomb structure. When applying the material models to a multi-strain  
469 rate and state application, a close correlation between predicted and experimental data was  
470 observed (Figure 10). The stress-softening characteristic of the Mullin's effect is evident  
471 when comparing Figure 6 and Figure 7. Even at a relatively low strain (0.4), the initial  
472 stiffness of the primary response is 31% higher than that of the stabilised response, and  
473 15% higher stress at maximum strain. This reinforces the importance of understanding and  
474 selecting the correct material response when simulating TPEs in specific applications. This  
475 study has also highlighted the need to characterise multiple responses for a single material,  
476 with both primary and stabilised responses being required to validate consecutive dynamic  
477 compressions of a honeycomb structure (Figure 10).

478

479 Good correlation was achieved between the HE material models and experimental data  
480 across both the primary ( $r^2 = 0.97$ ) and stabilised ( $r^2 = 0.99$ ) response. Such strong  
481 correlation provided a robust platform to investigate dynamic strain-rate applications. The  
482 low RMS error requirement placed on the stress relaxation data meant that the viscoelastic  
483 portion of the material model closely followed the experimental response. Consequently,

484 these material models accurately simulate NinjaFlex behaviour in dynamic applications of a  
485 similar strain (i.e. +/-0.3).

486

487 Applying the material model to the honeycomb structure achieved strong comparability  
488 between simulation and experimental data. This strong correlation validates this novel  
489 method for TPE characterisation, whilst also demonstrating the potential for use in complex  
490 geometries within dynamic environments. The mechanical response (Figure 10) and  
491 deformation patterns (Figure 11 and Figure 12) demonstrated excellent prediction of a  
492 complex HE buckling event. The quasistatic stabilised experimental and computational  
493 investigations exhibited the weakest correlation. This may be caused by the residual strain  
494 accumulated during stabilising loading cycles which, in combination with the fixed boundary  
495 condition created by the adhesive tape, resulted in a period of tensile loading as the actuator  
496 returned to the datum. Whilst this was noted and appropriately adjusted for during data  
497 analysis, this additional loading regime could have triggered a unique response within the  
498 material, meriting future investigation.

499 The experimental and simulated honeycombs exhibited discrepancies between their  
500 deformation patterns during dynamic loading (Figure 12). Whilst the honeycomb walls  
501 appeared to all form s-shaped profiles during experimental testing, a combination of s-  
502 shaped and inward folding behaviour was observed in the simulated deformation patterns.  
503 This appears to be focussed around the bending of the upper thick section's profile within  
504 the simulation, causing inward folding to occur underneath. **AM inherently results in wall**  
505 **thickness variation and, whilst the range of wall thickness was minimal and the simulated**  
506 **stress-strain behaviour correlated well with mechanical testing, the lack of this variability**  
507 **could have influenced the deformation pattern observed here.** Additionally, the buckling in  
508 the structures is a non-trivial event and, therefore, some deviation in deformation patterns  
509 was expected between the simulated and experimental behaviour. Structural response can  
510 also be influenced by contact behaviour; however, this study investigated pre-densification

511 behaviour and, when running these simulations with a general frictional contact (as opposed  
512 to frictionless), minimal change in stress-strain behaviour was observed.

513

514 This study assumed linear viscoelasticity and, whilst the use of non-linear viscoelastic  
515 models may help to further fine-tune the prediction of varying strain rate behaviour, this  
516 comes at a substantial computational time cost. In the light of this drawback, the close  
517 correlation of predicted behaviour presented here serves to justify the assumption of linear  
518 viscoelasticity. In the light of mainstream adoption due to low machine costing, fused  
519 filament fabrication (FFF) is considered by many to be a rudimentary/entry level technique.  
520 The potential of FFF to produce high quality components is, however, demonstrated here,  
521 with an excellent cuboid part density of 99.97%. This exceeds previously reported densities  
522 achieved via Selective Laser Sintering (SLS) TPE components (~95%) [16] and is  
523 comparable to Injection Moulded parts. Accounting for 94% of the cumulative pore volume,  
524 the largest voids (70-119 $\mu$ m) are technically challenging to eliminate in FFF builds and  
525 existed between the rectilinear fill and bounding outline of the cuboid. During tuning of  
526 processing parameters, attempts to reduce these voids included: use of concentric (instead  
527 of rectilinear) fill, increasing extrusion multiplier, and increasing overlap between the inner  
528 rectilinear fill and bounding outline. These methods introduced their own issues such as the  
529 concentric fill generating significant voids in the centre of the part, whilst increasing  
530 overlap/extrusion multiplier resulted in distortion of printing parts. **It should be noted that the  
531 threshold size of 20 $\mu$ m was selected to ensure the pores within the entirety of the cuboid  
532 could be captured in a single scan. Whilst this provides a suitable indicator of the porosity of  
533 the part (as the pores circa 70-110 $\mu$ m accounted for 94% of the measured pore volume),  
534 this has the potential to filter out smaller pores that could have an undetermined influence on  
535 material behaviour.**

536 It is known that the layer-by-layer AM build process produces component anisotropy, with  
537 this behaviour frequently noted in the literature perpendicular to the layer deposition [17-19].

538 This behaviour is highly dependent on manufacturing build quality as this logically effects the  
539 inter-layer bonding. As complex printed components can be exposed to different strain  
540 states, there exists the potential for loadings to be applied parallel and perpendicular to inter-  
541 layer bonding even if the overall structure is only under compressive loading. Due to the lack  
542 of notable voids, similar deformation patterns/mechanical responses and good correlation  
543 between stress-strain behaviour of the honeycomb structure, no further investigation of  
544 anisotropy was performed in this study.

545 As single-track parts (e.g. as per the honeycomb geometry) have no bonding between  
546 extrudate in-layer, they can have different mechanical responses than parts with infill  
547 patterning (e.g. test parts used to characterise NinjaFlex). Whilst the presence of minimal  
548 voids in the recti-linear fill pattern, good correlation between the simulated honeycomb  
549 response (using infill patterning characterisation) and mechanical testing (of single extrudate  
550 honeycomb print) all indicate this effect was not significant, poor optimisation of printer  
551 properties can lead to a disparity in these responses.

552 **5. Conclusions**

553

554 This study has achieved a greater understanding of the behaviour of TPE AM materials,  
555 enabling more effective exploitation of this emerging technology. A novel approach to  
556 efficiently and robustly characterise TPE materials has been presented. The importance of  
557 considering strain-softening has also been demonstrated, along with the potential to design  
558 and analyse AM structures for high performance applications. Highlighted findings include:

- 559 • Multi-state strain data to define a material model has been acquired using a standard  
560 uni-axial testing machine.
- 561 • A material model has been fitted to the TPE test data, including viscoelastic effects.  
562 This model is then successfully validated through its application to a case study of a  
563 traditional hexagonal honeycomb at varying strain rate.
- 564 • The level to which the TPE material was strained had significant effects on  
565 subsequent straining of the material, an important consideration when developing  
566 material models for applications involving multiple cycling events.
- 567 • When dynamically compressed, the viscoelastic properties significantly affect the  
568 recorded forces, demonstrating a significant degree of strain-rate dependence.  
569 These strain-rate effects carried over to the manufactured parts, resulting in a  
570 significant increase in recorded force when dynamically compressed, compared to  
571 quasistatic compression.
- 572 • FFF has been used to fabricate TPU components of high homogeneity (material  
573 density of 99.97%), with expected manufacturing considerations spreading material  
574 at the extruder nozzle, resulting in an increased wall thickness.

575

576

577 **6. Acknowledgements**

578

579 M. Robinson was supported by the Knowledge Economy Skills Scholarships 2 (via the  
580 Welsh Government's European Social Fund).

581 The X-ray imaging work was supported by the Advanced Imaging of Materials (AIM) facility  
582 (EPSRC grant no. EP/M028267/1), the European Social Fund (ESF) through the European  
583 Union's Convergence programme administered by the Welsh Government.

584

585 **7. Bibliography**

- 586 1. Huang, X., et al., *Topology optimization of microstructures of cellular materials and*  
587 *composites for macrostructures*. Computational Materials Science, 2013. **67**: p. 397-407.
- 588 2. Coelho, P.G., et al., *A hierarchical model for concurrent material and topology optimisation*  
589 *of three-dimensional structures*. Structural and Multidisciplinary Optimization, 2008. **35**(2):  
590 p. 107-115.
- 591 3. Brackett, D., I. Ashcroft, and R. Hague. *Topology optimization for additive manufacturing*. in  
592 *Proceedings of the solid freeform fabrication symposium, Austin, TX*. 2011. S.
- 593 4. Leary, M., et al., *Optimal topology for additive manufacture: a method for enabling additive*  
594 *manufacture of support-free optimal structures*. Materials & Design, 2014. **63**: p. 678-690.
- 595 5. Mullins, L., *Softening of Rubber by Deformation*. Rubber Chemistry and Technology, 1969.  
596 **42**(1): p. 339-362.
- 597 6. Mower, T.M. and M.J. Long, *Mechanical behavior of additive manufactured, powder-bed*  
598 *laser-fused materials*. Materials Science and Engineering: A, 2016. **651**: p. 198-213.
- 599 7. Gorse, S., et al., *Additive manufacturing of metals: a brief review of the characteristic*  
600 *microstructures and properties of steels, Ti-6Al-4V and high-entropy alloys*. Science and  
601 Technology of Advanced Materials, 2017. **18**(1): p. 584-610.
- 602 8. Wadley, H.N.G., N.A. Fleck, and A.G. Evans, *Fabrication and structural performance of*  
603 *periodic cellular metal sandwich structures*. Composites Science and Technology, 2003.  
604 **63**(16): p. 2331-2343.
- 605 9. Ajdari, A., H. Nayeb-Hashemi, and A. Vaziri, *Dynamic crushing and energy absorption of*  
606 *regular, irregular and functionally graded cellular structures*. International Journal of Solids  
607 and Structures, 2011. **48**(3-4): p. 506-516.
- 608 10. Day, J. and K. Miller, *Equibiaxial Stretching of Elastomeric Sheets, An Analytical Verification*  
609 *of an Experimental Technique*, in *ABAQUS users' conference*. 2000: Newport, RI. p. 205-220.
- 610 11. Ninjatek, *NinjaFlex® 3D Printing Filament*, in *Ninjatek Technical Specifications*, Ninjatek,  
611 Editor. 2016, Ninjatek.
- 612 12. Abueidda, D.W., et al., *Mechanical properties of 3D printed polymeric cellular materials with*  
613 *triply periodic minimal surface architectures*. Materials & Design, 2017. **122**: p. 255-267.
- 614 13. BSI, *BS ISO 37:2017 - Rubber, vulcanized or thermoplastic — Determination of tensile stress-*  
615 *strain properties*. 2017, BSI.
- 616 14. Treloar, L.R.G., *The physics of rubber elasticity*. 1975: Oxford University Press, USA.
- 617 15. Bergstrom, J.S., *Mechanics of solid polymers: theory and computational modeling*. 2015:  
618 William Andrew.
- 619 16. Dadbakhsh, S., et al. *Effect of powder size and shape on the SLS processability and*  
620 *mechanical properties of a TPU elastomer*. in *Physics Procedia*. 2016. Elsevier.
- 621 17. Frazier, W.E., *Metal Additive Manufacturing: A Review*. Journal of Materials Engineering and  
622 Performance, 2014. **23**(6): p. 1917-1928.
- 623 18. Soe, S.P., et al., *Mechanical characterisation of Duraform® Flex for FEA hyperelastic material*  
624 *modelling*. Polymer Testing, 2014. **34**: p. 103-112.
- 625 19. Ahn, S.-H., et al., *Anisotropic material properties of fused deposition modeling ABS*. Rapid  
626 prototyping journal, 2002. **8**(4): p. 248-257.

627